Towards artificial Ising spin glasses: Thermal ordering in randomized arrays of Ising-type nanomagnets

Michael Saccone,[1,*] Andreas Scholl,[2] Sven Velten,[3,4] Scott Dhuey,[5] Kevin Hofhuis,[6,7] Clemens Wuth,[4] Yen-Lin Huang,[8] Zuhuang Chen,[9] Rajesh V. Chopdekar,[2] and Alan Farhan[2,7,10,†]

[1]*Physics Department, University of California, 1156 High Street, Santa Cruz, California 95064, USA*
[2]*Advanced Light Source, Lawrence Berkeley National Laboratory (LBNL), 1 Cyclotron Road, Berkeley, California 94720, USA*
[3]*Materials Sciences Department, Lawrence Berkeley National Laboratory, 1 Cyclotron Road, Berkeley, California 94720, USA*
[4]*Institut für Nanostruktur- und Festkörperphysik, Universität Hamburg, Jungiusstraße 11, 20355 Hamburg, Germany*
[5]*The Molecular Foundry, Lawrence Berkeley National Laboratory (LBNL), 1 Cyclotron Road, Berkeley, California 94720, USA*
[6]*Laboratory for Mesoscopic Systems, Department of Materials, ETH Zurich, 8093 Zurich, Switzerland*
[7]*Laboratory for Multiscale Materials Experiments (LMX), Paul Scherrer Institut, 5232 Villigen, Switzerland*
[8]*Department of Materials Science and Engineering, University of California, Berkeley, California 94720, USA*
[9]*School of Materials Science and Engineering, Harbin Institute of Technology, Shenzhen, Guangdong 518055, China*
[10]*NanoSpin, Department of Applied Physics, Aalto University School of Science, P.O. Box 15100, FI-00076 Aalto, Finland*

(Received 11 February 2019; revised manuscript received 21 May 2019; published 3 June 2019)

We explore the thermodynamics in two-dimensional arrays consisting of Ising-type nanomagnets lithographically arranged onto random sites and angular orientations. Introducing these basic spin-glass ingredients, we study the characteristic features of the low-energy states achieved, following thermal-annealing protocols. From direct visualization of real-time dynamics, we record relaxation timescales together with magnetic susceptibility variations over temperature, revealing trends towards short-range order as randomness is increased, but falling short of pure spin-glass behavior. Our work provides a route towards the realization of artificial Ising spin-glass systems.

DOI: 10.1103/PhysRevB.99.224403

I. INTRODUCTION

Spin glasses are magnets exhibiting a random mixture of ferro- and antiferromagnetic order with frustrated spin formations, highly degenerate energy landscapes, and nontrivial pathways to their respective ground states [1]. In fact, the spin-glass ground-state question has long been an extensively investigated optimization problem [2,3]. The spin-glass phase transition, most prominently characterized by a sharp cusp in ac-susceptibility measurements, has been an area of intense research efforts since the early 1970's, both experimentally and theoretically [4]. The variety of characteristic phenomena in spin-glass systems has mostly been investigated using macroscopic or spectroscopic characterization techniques, ranging from magnetometry [5] and Mössbauer spectroscopy [6] to neutron diffraction and μSR spectroscopy [7]. Recent advances in nanofabrication techniques opened up a pathway to create artificial spin systems that exhibit geometrical frustration and allow direct real-space observations of magnetic configurations [8,9]. Artificial spin-ice systems [10], comprising Ising-type nanomagnets lithographically arranged onto two-dimensional square [9,11] and kagome [12,13] geometries, emerged as prominent examples in recent years. In particular, artificial spin ices exhibiting thermally induced moment fluctuations [14–16] paved the way for a whole new line of research, where Ising-type nanomagnets are arranged onto novel two-dimensional magnetically frustrated geometries, leading to emergent phenomena that do not necessarily exist in nature. Such phenomena range from emergent magnetic charge screening [17,18], emergent reduced dimensionality as a result of vertex frustration [19], and spin frustration that can be directly tuned at the nanoscale [20–22]. A common feature among all these artificial frustrated systems is their regular and ordered geometries. This raises the question of whether an artificial Ising spin-glass system can be created from the same Ising-type nanomagnets arranged into random and disordered patterns. If so, what types of magnetic configurations are accessed, following thermal-annealing protocols [15,18]? How would the directly observable thermal fluctuations behave, as temperature and disorder are varied? Can a two-dimensional spin glass be experimentally realized, despite theoretical predictions only discovering zero-temperature glass phases [23,24]?

In the present work, we aim to take a step in addressing these questions by fabricating arrays of nanomagnets exhibiting a controlled disorder and randomness, the major ingredient for the emergence of spin-glass behavior. We begin with a methods section that describes the sample fabrication process and the sample characterization, employing synchrotron-based photoemission electron microscopy (PEEM). Then, we move on to a section describing the obtained results, starting from thermal-annealing experiments and

*msaccone@ucsc.edu
†alan.farhan@gmx.net

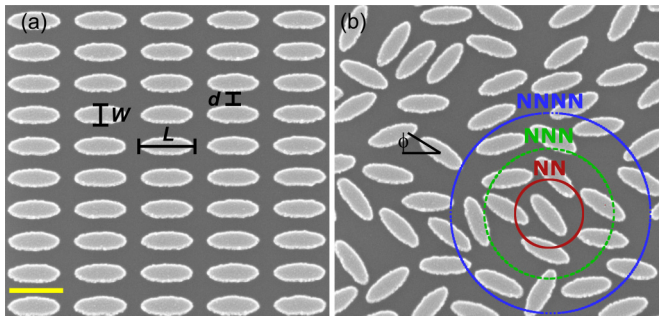

FIG. 1. (a) Scanning electron microscope (SEM) image of part of an arrangement consisting of Ising-type nanomagnets with length $L = 300$ nm, width $W = 100$ nm, and thickness $t = 2.7$ nm arranged onto a collinear ordered fashion with a nearest-neighbor edge-to-edge distance $d = 80$ nm. (b) SEM image of an array, where disorder in the x and y coordinates of the centers of nanomagnets is introduced in the form of Gaussian distribution with a relative deviation $\sigma = 100\%$ around an average edge-to-edge distance of $d = 80$ nm. In addition to coordinate randomness, the same type of disorder is introduced for the rotational angle ϕ, ensuring maximum randomness possible in two dimensions. Circles representing the area in which spins will be designated nearest neighbor (NN, red line), next-nearest neighbor (NNN, green dashed line), and next-next-nearest neighbor (NNNN, blue dotted line) are drawn to denote categories used to calculate correlation functions.

temperature-dependent moment fluctuations observed in randomized nanomagnetic patterns. We then conclude with a section summarizing the obtained results with conclusions and an outlook for potential future work.

II. METHODS

The samples were fabricated by lift-of–assisted electron-beam lithography. A $1 \times 1\,\mathrm{cm}^2$ silicon (100) substrate was first spin coated with a 70-nm-thick layer of polymethylmethacrylate (PMMA) resist. Patterns of interest are then exposed on the substrate using a VISTEC VB300 electron-beam writer. Next, a 2.7-nm-thick ferromagnetic permalloy ($Ni_{80}Fe_{20}$) film was thermally evaporated at a base pressure of 1.4×10^7 torr, together with 1.5-nm-thick aluminum capping layer, to avoid fast oxidation of the structures. This was followed by lift-off in acetone at a temperature of 50 °C. The resulting nanomagnets had lengths $L = 300$ nm and widths $W = 100$ nm [see Figs. 1(a) and 1(b)]. The elongated shape of the patterned single-domain nanomagnets are chosen so that the magnetization within each individual nanomagnet can only point in one of two possible direction along the long axis of the nanomagnet. Thus, each nanomagnet represents an individual Ising macrospin. The nanomagnet dimensions are chosen to ensure a blocking temperature T_B of 190–240 K. Generally, we define the blocking temperature as the temperature where thermally induced moment reorientations of the nanomagnets start to occur at the timescale of several seconds [18,20].

To introduce a controlled disorder in the lattice, the islands are shifted from their lattice site, as depicted in Fig. 1. The shift is controlled by separate Gaussian distributions along the x and y directions. Thereby, the average and standard deviations in x (y) coordinates are given by the perfect lattice sites and by $\sigma_{\mathrm{abs}}{=}\sigma[(W, L) + d]$, with σ defined as the relative deviation, W (L) the width (length) of the islands, and d the average edge-to-edge distance. Introducing disorder in the x and y coordinates results in patterns consisting of horizontal (nonrotated) nanomagnets arranged at random x and y sites. For simplicity, we call these structures the *nonrotated* arrays. Further disorder is induced by introducing the same type of randomness to the orientational angle ϕ of the nanomagnets [see Fig. 1(b)]. The rotational distribution is defined around zero degrees (islands are aligned along the x axis) with a deviation of $\sigma_\phi = 180°\sigma$. Since x-ray magnetic circular dichroism (XMCD) contrast in the X-PEEM experiments is angle sensitive [25] with maximum contrast, when an angle of 0° is present between the incoming x rays and the magnetization direction (zero contrast is present for an angle of 90°), the rotation of the nanomagnets is limited to a maximum of 80°. Again, for simplicity, we call these patterns with additional rotational disorder the *rotated* arrays. Three kinds of disorder are investigated, i.e., $\sigma = 0\%$ (ordered), 30% (distorted), and 100% (disordered), for an edge-to-edge distance $d = 80$ nm. Furthermore, to ensure that nanomagnets do not overlap as a result of the introduced randomness, we define a minimum of 20 nm edge-to-edge distance when generating the random patterns. This minimum edge-to-edge distance also ensures a smooth and clean lift-off process in acetone. The overall number of nanomagnets in each individual array was 7200, occupying areas of 26–30 $\mu\mathrm{m}^2$. These system sizes are comparable to previously studied artificial frustrated spin systems [15,18,20], reducing potential finite-size effects to a negligible minimum.

Magnetic imaging was performed at PEEM3 [26] at the Advanced Light Source, employing XMCD at the Fe L_3 edge [27]. XMCD images are obtained by pixelwise division of images recorded with right and left circularly polarized x rays. The resulting XMCD contrast gives a direct measure of the projection of the magnetic moments onto the x-ray propagation vector. Moments pointing towards the incoming x rays will appear dark, while moments opposing the x-ray direction will appear bright [see Figs. 2(a)–2(e)]. For each x-ray polarization, an exposure time of one-and-a-half seconds is chosen, while switching polarizations regularly takes four seconds. This gives an overall time of roughly seven seconds to obtain an XMCD image. The aforementioned blocking temperature is chosen to fit these timescales.

III. RESULTS

A. Thermal annealing

As mentioned above, we aim to explore the effect of increasing disorder and randomness on low-energy magnetic moment configurations achieved after thermal-annealing protocols [18–20]. For that purpose, the sample is heated *in situ* up to 350 K, where it is kept for 1–2 hours. Then, the sample is cooled down to 180 K for magnetic imaging of both time-dependent dynamics and low-temperature states [see Figs. 2(a)–2(e)]. At these low temperatures, the moment configurations are not observed to change over time and appear to be in a frozen state. Following this annealing procedure, the regular arrays [see Fig. 1(a)] show

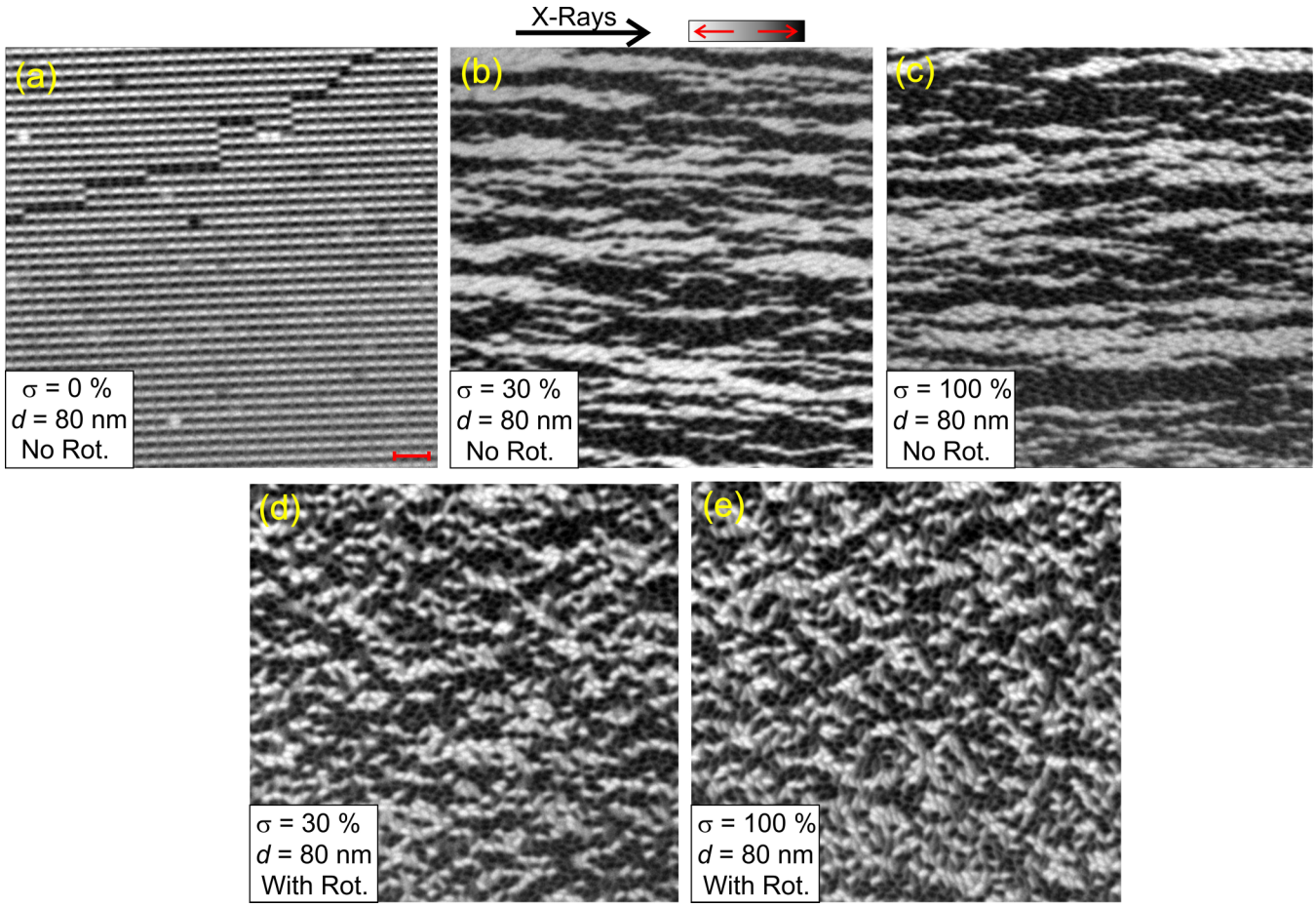

FIG. 2. XMCD images of a low-energy moment configuration achieved, following thermal annealing in (a) a fully ordered array of Ising-type nanomagnets, (b) a partially randomized array ($\sigma = 30\%$) of parallel nanomagnets (no rotational disorder), (c) a fully randomized array ($\sigma = 100\%$) of parallel nanomagnets (no rotational disorder), (d) a partially randomized array ($\sigma = 30\%$) with rotational disorder, and (e) a fully randomized array ($\sigma = 100\%$) with rotational disorder. The red scale bar indicates 1 μm. We see a transition from (a) a long-range-ordered antiferromagnetic moment alignment for the ordered arrays, showing the characteristic dark and bright lines, to (b),(c) a long-range-ordered ferromagnetic state for the arrays with only positional disorder, ending in (d),(e) short-range-ordered phases, when full randomness is introduced with rotational disorder.

long-range-ordered ground-state patterns consisting of antiferromagnetic moment alignments, seen as black and white stripes in the XMCD images [see Fig. 2(a)]. Considering the dipolar nature of internanomagnet interactions, these moment configurations are not surprising [28]. Interestingly, this antiferromagnetic alignment of moments transforms into long-range-ordered configurations exhibiting domains of parallel (or ferromagnetic) moment alignments [see dark and bright patches in Figs. 2(b) and 2(c)] for arrays with nanomagnets where randomization is induced for the x and y coordinates, but where all nanomagnets remain nonrotated [see Figs. 2(b) and 2(c)]. Introducing rotational randomness of the Ising-type nanomagnets, as described above, leads to more complex ordering patterns [dark and bright domains in Figs. 2(d) and 2(e)], which at least visually appear more short-range ordered compared to the nonrotated arrays.

To quantify this ordering, the spatial correlation function, conventional in the analysis of ferromagnets and antiferromagnets, was calculated,

$$C(\mathbf{r}_{ij}) = \langle S_i S_j \rangle_T, \tag{1}$$

where $S_i = \pm 1$ to represent the Ising state of spin i, r_{ij} is the distance between spins i and j, and $\langle \cdots \rangle_T$ denotes a thermal average. The absolute value of this, $C'(\mathbf{r}_{ij}) = |C(\mathbf{r}_{ij})|$, was used for correlation function calculations. After days at room temperature and subsequent gradual cooling, the systems are assumed to be in equilibrium, thus allowing/enabling one to take the thermal average over time (in the temperature-dependent case). This average is not possible for the annealed, frozen configurations as only one state of the system was accessed after each annealing procedure. To perform a meaningful average for a single spin configuration and more effectively extract correlation lengths in the thermally active cases, a set of bins at evenly spaced values r was chosen. All correlation function values corresponding to $r - \Delta/2 < r_{ij} < r + \Delta/2$, where Δ is the distance between consecutive r_k, were averaged to a single value,

$$[C'(r)]_{av} = \frac{1}{N_{\text{pair}}} \sum_{ij}{}' C'(\mathbf{r}_{ij}). \tag{2}$$

TABLE I. Correlation length ξ and magnetic susceptibility χ for magnetic configurations achieved after thermal annealing, all summarized as a function of increasing disorder σ for structures without and with rotational disorder. The third column represents the correlation length as multiples of the largest dimension of the islands, L, for greater clarity of interpretation. The first two digits of the values are displayed due to imprecision from the limited sample size.

Lattice type	ξ (μm)	ξ/L	χ
Nonrotated $\sigma = 0\%$	7.6	25	0.0×10^{-12}
Nonrotated $\sigma = 30\%$	3.1	10	2.4×10^{-12}
Nonrotated $\sigma = 100\%$	3.9	13	1.8×10^{-12}
Rotated $\sigma = 30\%$	1.2	4.1	1.7×10^{-12}
Rotated $\sigma = 100\%$	1.3	4.3	1.5×10^{-12}

The fit of the function to the exponential, $[C'(r)]_{av} = \exp(-r/\xi)$, with ξ being the so-called correlation length, produced the values given in Table I (see also Figs. 3(a) and 3(c)). Notably, this is an order parameter that does not always diverge with spin-glass transition [24,29]. The proper spin-glass correlation function is believed to be [24]

$$C_{SG}(\mathbf{r}_{ij}) = \langle S_i S_j \rangle^2. \tag{3}$$

This function would always possess the value of one for the frozen configurations of spins, and therefore provides no information about them. For the time-dependent measurements that allowed a spatial average,

$$[C_{SG}(r)]_{av} = \frac{1}{N_{\text{pair}}} \sum_{ij}{}' C_{SG}(\mathbf{r}_{ij}), \tag{4}$$

all values of this function were within their error bars from zero while $i \neq j$. Though short-range correlations are likely present, this information is obscured by the current statistics.

These measures of correlation do not discern whether the system is ferro- or antiferromagnetically correlated. Therefore, a "neighbor" correlation function is introduced:

$$[C]_{\text{N}} = \frac{1}{N_{\text{pair}}} \sum_{ij}^{\text{N}} C(\mathbf{r}_{ij}), \tag{5}$$

where the sum was either taken over nearest-neighbor (NN, $r_{ij} \leqslant 180$ nm), next-nearest-neighbor (NNN, $180 < r_{ij} \leqslant 360$ nm), or next-next-nearest neighbor (NNNN, $360 < r_{ij} \leqslant 540$ nm) pairs [see Fig. 1(b) for an illustration of these regions]. Since the geometry of these systems is variable, this does not strictly represent nearest-neighbor coupling in a traditional sense, but does provide a consistent basis for measuring local correlations. A value below zero indicates predominantly antiferromagnetic coupling, while one above zero indicates ferromagnetic coupling. These correlations are plotted for all systems of interest in Figs. 3(b) and 3(d) and

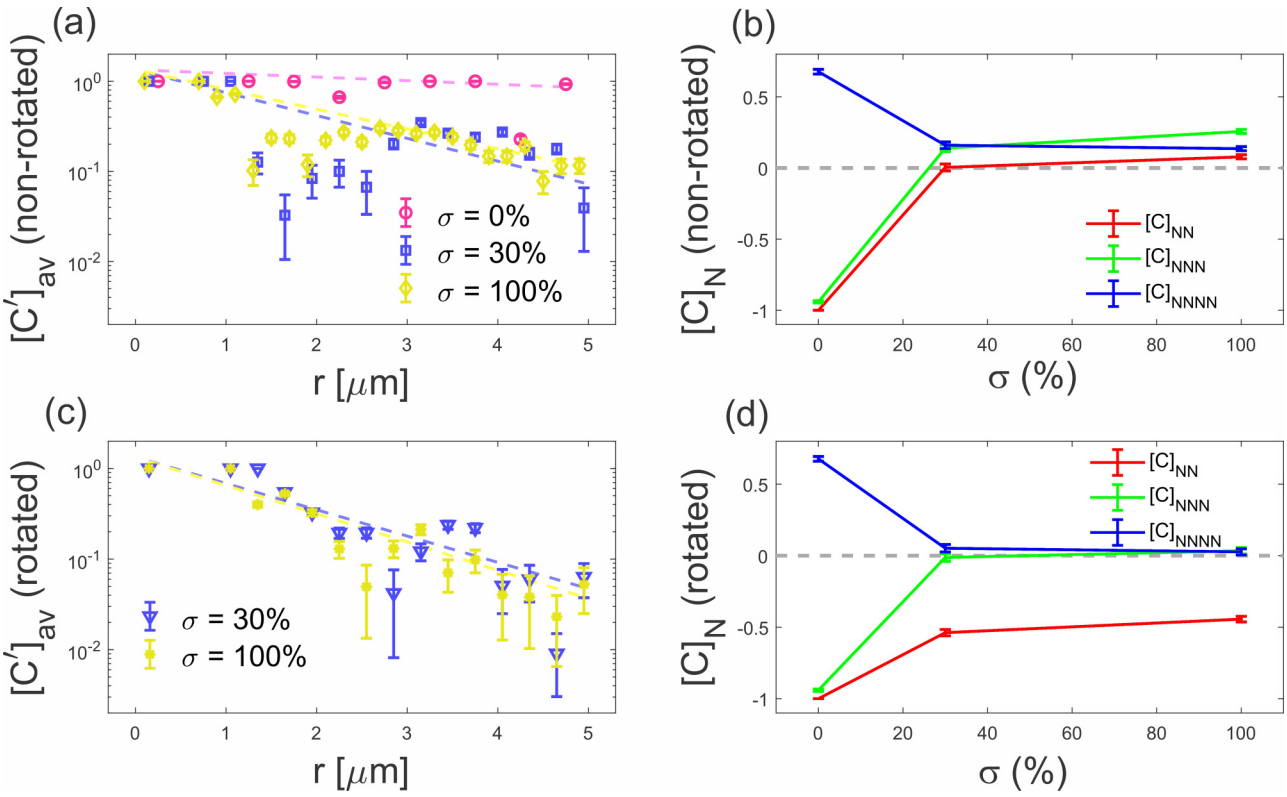

FIG. 3. Measures of correlation in the annealed systems. On the left are the absolute values of the spatial correlation functions from the (a) nonrotated and (c) rotated samples plotted on a semilogarithmic scale with their exponential fits indicated with dashed lines. (a) The nondisordered (magenta circles), partially disordered (blue squares), and fully disordered (yellow diamonds) nonrotated cases; (c) the partially (blue triangles) and fully (yellow stars) disordered rotated systems. The dotted lines represent the fits used to extract the correlation lengths. On the right are the nearest-neighbor correlations of the (b) nonrotated and (d) rotated systems as disorder is varied.

confirm qualitative observations of XMCD images such as in Fig. 2. The alternating left-oriented stripes and right-oriented stripes of magnetic moments in the ordered system give rise to NN and NNN antiferromagnetic ordering and NNNN ferromagnetic ordering [see $\sigma = 0$ in Figs. 3(b) and 3(d)]. When position alone is disordered, NN ordering becomes approximately evenly split, as the correlation measure approaches a value of zero [red line in Fig. 3(b)], while NNN and NNNN ordering is weakly ferromagnetic, strengthening with higher disorder [see Fig. 3(b)]. The internanomagnet coupling prefers ferromagnetic-type coupling when spins are moved away from their ordered state. This is mainly due to the fact that the tips of the nanomagnets exhibit the strongest interaction among each other. So, adding positional disorder leads to an increase in colinear (ferromagnetic) ordering patterns. The tip-to-tip aligned spins interact ferromagnetically by their geometry and with greater strength than antiferromagnetic spins aligned side to side. In other words, nanomagnets that have their ends facing each other exhibit a stronger ferromagnetic-type coupling than nanomagnets that are perfectly parallel to one another, which exhibit a weaker antiferromagnetic coupling. A similar effect is observed in the so-called dipolar trident lattice [20]. When rotation is introduced, however, this trend disappears. Due to the orientations changing, there is a smaller probability that these strong tip-to-tip interactions will be accessed. Antiferromagnetic order dominates for the NN interactions, but equalizes for the NNN and NNNN interactions [see Fig. 3(d)]. These orderings influence the critical behavior of the system as is further revealed by the temperature-dependent measurements discussed in the next section.

The dimensionless magnetic susceptibility χ was calculated from this correlation using the fluctuation-dissipation theorem [30]. This susceptibility χ was returned to appropriate dimensions by an additional factor m (the magnetic moment of a single spin, referred to as μ in the source):

$$\chi = \frac{m^2}{k_B T} \sum_{ij} C(\mathbf{r}_{ij}). \tag{6}$$

For the arrays discussed here, the magnetic moment m is calculated from a saturation magnetization, $M = 85$ kA/m, found for similarly thin-film permalloy kagome structures [25], to be $m = 5.41 \times 10^{-18}\,\mathrm{Am}^2$. The susceptibility was extracted from the annealed configurations of all samples at 180 K (Table I). The ordered case shows an essentially vanishing susceptibility as the true ground state of this system corresponds to $\chi = 0$. All other systems decrease in susceptibility and increase in correlation length with increasing disorder. This suggests that the higher density, strongly interacting areas introduced by disorder may create isolated clusters of correlated spin. These clusters are less susceptible to external fields due to their strong interactions with close neighbors.

B. Temperature-dependent moment fluctuations

Now, we turn to our attention to temperature-dependent observations of thermal fluctuations in our artificial Ising spin-glass structures [31]. To further explore the effects of disorder, the characteristic relaxation time τ of both rotated and nonrotated systems is explored, with a focus on arrays with the highest degree of introduced disorder ($\sigma = 100\%$) and freezing temperatures between 230 and 240 K [see teal dotted lines in Figs. 4(a)–4(f)]. Below these temperatures, only a few spin islands fluctuated due to disorder intrinsic to the fabrication process. In studies of magnetic nanowires and nanomagnetic spin systems, intrinsic disorder can generate spatial disorder that pins domain walls [32,33]. While this disorder can be expected for any patterned thin film, no domain pinning effects were apparent in the time evolution of the systems discussed here, which can be seen in two movies in the Supplemental Material [31]. In a spin-glass phase, the relaxation timescale is not expected to remain constant over

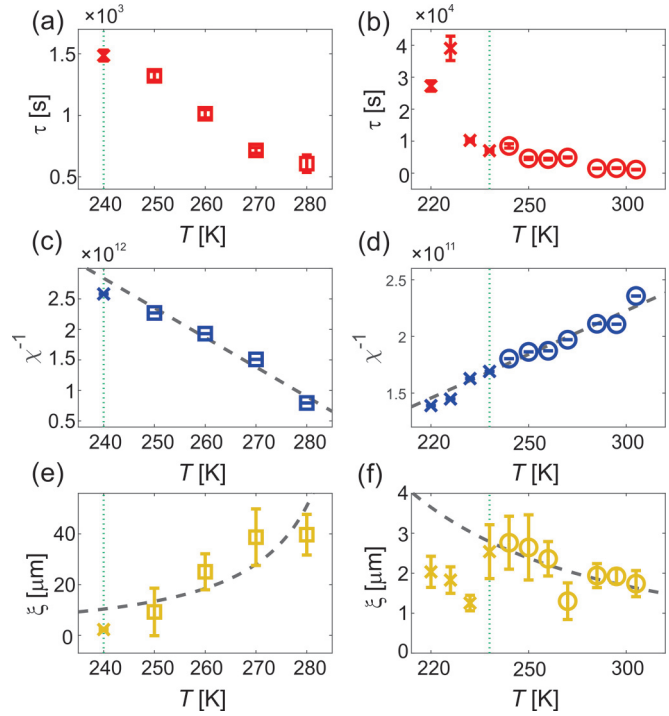

FIG. 4. Temperature dependence of (a),(c),(e) the nonrotated $\sigma = 100\%$ system and (b),(d),(f) the rotated $\sigma = 100\%$ system. The data points at and to the left of the teal dotted vertical lines are marked with crosses to indicate that they come from frozen configurations of spin islands. (a),(b) The characteristic relaxation time τ was recorded from a least-squares fit of the autocorrelation function [Eq. (6)]. The error bars are the standard error of this fit. (c),(d) The dimensionless magnetic susceptibility for nonrotated and rotated patterns, respectively. χ was extracted from the spatial correlation function [Eq. (5)] at each frame. The averages from all frames are plotted with error bars representing standard deviations of the mean. The decreasing inverse susceptibility for nonrotated patterns (blue squares) indicate long-range ferromagnetic ordering, which is also visually evident in Fig. 2(b). The gray dashed lines in (c) and (d) are the linear Curie-Weiss fit, which imply critical temperatures of $T_c = 298 \pm 28.8$ K for the nonrotated patterns and $T_c = 11.2 \pm 14.9$ K for the rotated patterns. (e),(f) The least-squares fit to the spatial correlation function [Eq. (2)] produces the correlation length ξ, whose standard error is represented by the error bars. The curves of best fit plotted as gray dashed lines correspond to critical exponents of $\nu = 1.38 \pm 0.620$ for the nonrotated case and $\nu = 1.82 \pm 0.986$ for the rotated case.

time [34]. XMCD imaging provides the unique opportunity to directly observe this relaxation process and extract these relaxation timescales. The autocorrelation function,

$$C''(t) = \langle S(t)S(t_0)\rangle, \tag{7}$$

where the average is taken over all spins in the system, was measured from an initial time t_0 through a time 1200 seconds later and fit the curves to an exponential decay, $C''(t) = \exp(-t/\tau)$, revealing the so-called characteristic relaxation time τ at each temperature [see Figs. 4(a) and 4(b)]. The Pearson χ^2 goodness-of-fit tests [35] indicated that all fits to this curve rejected the null hypothesis with 95% confidence. With only a 5% chance that this model matched the data due to random fluctuation, this result strongly implies single timescale dynamics, inconsistent with the varying timescales found in the glass phase. As seen in Figs. 4(a) and 4(b), τ varies inversely with temperature as expected, but shows no indication of a spin-glass transition.

Furthermore, using the fluctuation-dissipation theorem from Eq. (5), the magnetic susceptibility was calculated at each temperature for both nonrotated and rotated arrays, and plotted in Figs. 4(c) and 4(d), respectively. The nonrotated patterns show a decreasing inverse susceptibility with increasing temperature [see Fig. 4(c)], indicating that the system is well within a long-range-ordered ferromagnetic phase, as can be visually seen from the XMCD image in Fig. 2(b). The opposite trend is observed for rotated structures [see Fig. 4(d)]. Applying a Curie-Weiss fit, $\chi = \frac{C}{T-T_c}$, to both temperature dependencies, where C is the Curie constant and T_c is the critical temperature, yields $T_c = 298 \pm 28.8$ K for the nonrotated patterns and $T_c = 11.2 \pm 14.9$ K for the rotated structures. This and all additional fits passed Pearson's χ^2 test. These temperatures differ by an order of magnitude due to the variable interaction strengths. Those strengths are higher for the nonrotated systems because the tips are more likely to be close to one another. This highlights the potential of controlling critical temperatures through a variation of certain parameters such as disorder σ, in our particular case.

Plotting the correlation lengths as function of temperature [see Figs. 4(e) and 4(f)], the data is fitted to a power law $\xi(T) = A((T - T_c)/T_c)^{\nu}$ using the T_c determined from the susceptibility and leaving A, a prefactor, and ν, the critical exponent, as fitting parameters. The gray dashed lines in Figs. 4(e) and 4(f) represent these fits, $\nu = 1.38 \pm 0.620$ and $\nu = 1.82 \pm 0.986$, for the rotated and nonrotated patterns, respectively. Comparing these exponents to those of the two-dimensional (2D) and 3D spin glasses ($\nu = 3.559 \pm 0.025$ [36] and $\nu = 2.15(15)$ [37], respectively) and the 2D through 4D Ising models ($\nu = 1$, $\nu = 0.6310 \pm 0.0015$, and $\nu = 0.5$ for two, three, and four dimensions, respectively [38]) further indicates that the systems investigated here, while exhibiting complex behavior, are not forming spin-glass phases. The critical exponent falls below the spin-glass critical exponents for two ($\nu = 3.559 \pm 0.025$ [36]) and three dimensions ($\nu = 2.15(15)$ [37]) and, considering the error, lies somewhere in the vicinity of the two-dimensional Ising model ($\nu = 1$ [38]).

IV. SUMMARY AND OUTLOOK

Seen as a whole, these systems do not form typical spin glasses, but offer hints as to how artificial spin glasses may be constructed. The random configurations should balance ferromagnetic and antiferromagnetic interaction to avoid ordering by either of those dominant behaviors. Patterning nanomagnet arrays to mimic higher-dimensional behaviors may achieve this, perhaps through concepts such as effective dimension [39]. If interactions are structured to be more treelike, then spin glasses can approach system-wide correlation in multiple configurations. This would translate to higher entropies corresponding to higher critical temperatures. System geometry may be modified further by randomizing spin dilution or nanomagnet sizes [40], or by introducing random height offsets [16,41] within the system. These modifications could leverage the long-range nature of dipolar interactions to shape interaction structures in methods not typically approached by purely theoretical studies. The patterned permalloy thin films analyzed here and in so-called artificial spin ices always exhibit an obstacle in the form of finite blocking temperatures, but nonzero critical temperatures would work around this limitation. Once these steps are taken and spin-glass phases are realized, the real-time dynamics of such artificial spin glasses may be explored in their entirety. This unique testing grounds could probe new questions about magnetic dynamics and systems with similar mathematic descriptions, such as artificial neural networks [42], electroencephalography (EEG) data [43], and sediment deposition [24]. Furthermore, the exploration of various temperature schedules and their effect on the low-energy state achieved [3], aging, and memory effects [1,4] in prospective artificial spin glasses will be the focus of potential future research, establishing direct links to naturally occurring spin-glass systems.

ACKNOWLEDGMENTS

The authors would like to thank A. P. Young, P. Fischer, A. Ramirez, C. F. Petersen, R. Streubel, and G. Meier for their support and fruitful discussions. This work was supported by the Swiss National Science Foundation (Projects No. 167642 and No. 174306) and part of this work was performed at the Advanced Light Source (ALS) and the Molecular Foundry, Lawrence Berkeley National Laboratory (LBNL). The Advanced Light Source and the Molecular Foundry are supported by the Director, Office of Science, Office of Basic Energy Sciences, of the U.S. Department of Energy under Contract No. DE-AC02-05CH11231.

[1] K. Binder and A. P. Young, Rev. Mod. Phys. **58**, 801 (1986).
[2] D. Sherrington and S. Kirkpatrick, Phys. Rev. Lett. **35**, 1792 (1975).
[3] G. S. Grest, C. M. Soukoulis, and K. Levin, Phys. Rev. Lett. **56**, 1148 (1986).
[4] J. A. Mydosh, Rep. Prog. Phys. **78**, 052501 (2015).
[5] P. Amornpitoksuk, D. Ravot, A. Mauger, and J. C. Tedenac, Phys. Rev. B **77**, 144405 (2008).
[6] M. Reissner, W. Steiner, Z. Seidov, G. Guseinov, Hyperfine Interact. **169**, 1305 (2006).

[7] V. K. Anand, D. T. Adroja, A. D. Hillier, J. Taylor, and G. André, Phys. Rev. B **84**, 064440 (2011).

[8] Y. Han, Y. Shokef, A. M. Alsayed, P. Yunker, Tom C. Lubensky, and A. G. Yodh, Nature (London) **456**, 898 (2008).

[9] R. F. Wang, C. Nisoli, R. S. Freitas, J. Li, W. McConville, B. J. Cooley, M. S. Lund, N. Samarth, C. Leighton, V. H. Crespi, and P. Schiffer, Nature (London) **439**, 303 (2006).

[10] C. Nisoli, R. Moessner, and P. Schiffer, Rev. Mod. Phys. **85**, 1473 (2013).

[11] J. P. Morgan, A. Stein, S. Langridge, and C. H. Marrows, Nat. Phys. **7**, 75 (2011).

[12] S. Ladak, D. E. Read, G. K. Perkins, L. F. Cohen, and W. R. Branford, Nat. Phys. **6**, 359 (2010).

[13] N. Rougemaille, F. Montaigne, B. Canals, A. Duluard, D. Lacour, M. Hehn, R. Belkhou, O. Fruchart, S. El Moussaoui, A. Bendounan, and F. Maccherozzi, Phys. Rev. Lett. **106**, 057209 (2011).

[14] V. Kapaklis, U. B. Arnalds, A. Farhan, R. V. Chopdekar, A. Balan, A. Scholl, L. J. Heyderman, and B. Hjörvarsson, Nat. Nanotechnol. **9**, 514 (2014).

[15] A. Farhan, P. M. Derlet, L. Anghinolfi, A. Kleibert, and L. J. Heyderman, Phys. Rev. B **96**, 064409 (2017).

[16] A. Farhan, M. Saccone, C. F. Petersen, S. Dhuey, R. V. Chopdekar, Y.-L. Huang, N. Kent, Z. Chen, M. J. Alava, T. Lippert, A. Scholl, and S. van Dijken, Sci. Adv. **5**, eaav6380 (2019).

[17] I. Gilbert, G.-W. Chern, S. Zhang, L. O' Brien, B. Fore, C. Nisoli, and P. Schiffer, Nat. Phys. **10**, 670 (2014).

[18] A. Farhan, A. Scholl, C. F. Petersen, L. Anghinolfi, C. Wuth, S. Dhuey, R. V. Chopdekar, P. Mellado, M. J. Alava, and S. van Dijken, Nat. Commun. **7**, 12635 (2016).

[19] I. Gilbert, Y. Lao, I. Carrasquillo, L. O' Brien, J. D. Watts, M. Manno, C. Leighton, A. Scholl, C. Nisoli, and P. Schiffer, Nat. Phys. **12**, 162 (2016).

[20] A. Farhan, C. F. Petersen, S. Dhuey, L. Anghinolfi, Q.- H. Qin, M. Saccone, S. Velten, C. Wuth, S. Gliga, P. Mellado, M. J. Alava, A. Scholl, and S. van Dijken, Nat. Commun. **8**, 995 (2017).

[21] C. F. Petersen, A. Farhan, S. Dhuey, Z. Chen, M. J. Alava, A. Scholl, and S. van Dijken, Appl. Phys. Lett. **112**, 092403 (2018).

[22] E. Östman, H. Stopfel, I.-A. Chioar, U. B. Arnalds, A. Stein, V. Kapaklis, and Bj. Hjörvarsson, Nat. Phys. **14**, 375 (2018).

[23] A. K. Hartmann and A. P. Young, Phys. Rev. B **64**, 180404(R) (2001).

[24] L. Berthier and G. Biroli, Rev. Mod. Phys. **83**, 587 (2011).

[25] A. Farhan, P. M. Derlet, A. Kleibert, A. Balan, R. V. Chopdekar, M. Wyss, L. Anghinolfi, F. Nolting, and L. J. Heyderman, Nat. Phys. **9**, 375 (2013).

[26] A. Doran, M. Church, T. Miller, G. Morrison, A. T. Young, and A. Scholl, J. Electron. Spectrosc. Relat. Phenom. **185**, 340 (2012).

[27] J. Stöhr, Y. Wu, B. D. Hermsmeier, M. G. Samant, G. R. Harp, S. Koranda, D. Dunham, and B. P. Tonner, Science **259**, 658 (1993).

[28] U. B. Arnalds, J. Chico, H. Stopfel, V. Kapaklis, O. Bärenbold, M. A. Verschuuren, U. Wolff, V. Neu, A. Bergman, and B. Hjörvarsson, New J. Phys. **18**, 023008 (2016).

[29] C. Dasgupta, A. V. Indrani, S. Ramaswamy, and M. K. Phani, Europhys. Lett. **15**, 307 (1991).

[30] S. G. Abaimov, *Statistical Physics of Non-Thermal Phase Transitions* (Springer, Cham, 2015), Vol. 1, pp. 289–364.

[31] See Supplemental Material at http://link.aps.org/supplemental/10.1103/PhysRevB.99.224403 for supplemental movie S1: XMCD image sequence of thermally induced moment fluctuations in an array with positional disorder $\sigma = 100\%$ recorded at 270 K, and supplemental movie S2: XMCD image sequence of thermally induced moment fluctuations in an array with positional and rotational disorder $\sigma = 100\%$ recorded at 300 K.

[32] S. Ladak, D. E. Read, W. R. Branford, and L. F. Cohen, New J. Phys. **13**, 023023 (2011).

[33] J. P. Morgan, A. Stein, S. Langridge, and C. H. Marrows, New J. Phys. **13**, 105002 (2011).

[34] Ph. Refregier, E. Vincent, J. Hammann, and M. Ocio, J. Phys. **48**, 1533 (1987).

[35] J. Taylor, *Introduction to Error Analysis, The Study of Uncertainties in Physical Measurements* (University Science Books, Mill Valley, 1997), Vol. 2, pp. 261–283.

[36] H. Rieger, L. Santen, U. Blasum, M. Diehl, M. Jünger, and G. Rinaldi, J. Phys. A: Math. Gen. **29**, 3939 (1996).

[37] H. G. Ballesteros, A. Cruz, L. A. Fernández, V. Martín-Mayor, J. Pech, J. J. Ruiz-Lorenzo, A. Tarancón, P. Téllez, C. L. Ullod, and C. Ungil, Phys. Rev. B **62**, 14237 (2000).

[38] J. C. Le Guillou and J. Zinn-Justin, J. Phys. **48**, 19 (1987).

[39] L. Daqing, K. Kosmidis, A. Bunde, and S. Havlin, Nat. Phys. **7**, 481 (2011).

[40] M. J. Morrison, T. R. Nelson, and C. Nisoli, New J. Phys. **15**, 045009 (2013).

[41] Y. Perrin, B. Canals, and N. Rougemaille, Nature (London) **540**, 410 (2016).

[42] J. J. Hopfield, Proc. Natl. Acad. Sci. **81**, 3088 (1982).

[43] A. G. Hudetz, C. J. Humphries, and J. R. Binder, Front. Syst. Neurosci. **8**, 234 (2014).